Thermospheric recovery during the 5 April 2010 geomagnetic storm

Sheng, Cheng; Lu, Gang; Solomon, Stanley C.; Wang, Wenbin; Doornbos, Eelco; Hunt, Linda A.; Mlynczak, Martin G.

DOI
10.1002/2016JA023520

Publication date
2017

Document Version
Final published version

Published in
Journal Of Geophysical Research-Space Physics

AGU PUBLICATIONS

JGR

Journal of Geophysical Research: Space Physics

RESEARCH ARTICLE
10.1002/2016JA023520

Thermospheric recovery during the 5 April 2010 geomagnetic storm

Cheng Sheng[1], Gang Lu[1], Stanley C. Solomon[1], Wenbin Wang[1], Eelco Doornbos[2], Linda A. Hunt[3], and Martin G. Mlynczak[3]

[1]High Altitude Observatory, National Center for Atmospheric Research, Boulder, Colorado, USA, [2]Aerospace Engineering, Delft University of Technology, Delft, Netherlands, [3]NASA Langley Research Center, Hampton, Virginia, USA

Key Points:
- The sensitivity of thermospheric temperature and density recovery rates after storms to nitric oxide cooling is tested
- Using the Duff et al. reaction rate for N(2D) + O2 in the TIEGCM improves agreement with recovery rates obtained from satellite observations
- The nitric oxide cooling rate is not very sensitive to the characteristic energy of auroral precipitation for the event studied

Supporting Information:
- Supporting Information S1

Correspondence to:
C. Sheng,
csheng@ucar.edu

Citation:
Sheng, C., G. Lu, S. C. Solomon, W. Wang, E. Doornbos, L. A. Hunt, and M. G. Mlynczak, (2017), Thermospheric recovery during the 5 April 2010 geomagnetic storm, *J. Geophys. Res. Space Physics*, *122*, 4588–4599, doi:10.1002/2016JA023520.

Received 26 SEP 2016
Accepted 15 MAR 2017
Accepted article online 3 APR 2017
Published online 18 APR 2017

Abstract Thermospheric temperature and density recovery during the 5 April 2010 geomagnetic storm has been investigated in this study. Neutral density recovery as revealed by Thermosphere-Ionosphere-Electrodynamics General Circulation Model (TIEGCM) simulations was slower than observations from GOCE, CHAMP, and GRACE satellites, suggesting that the cooling processes may not be fully represented in the model. The NO radiative cooling rate in TIEGCM was also compared with TIMED/SABER measurements along satellite orbits during this storm period. It was found that the model overestimated the NO cooling rate at low latitudes and underestimated it at high latitudes. The effects of particle precipitation on NO number density and NO cooling rate at high latitudes were examined in detail. Model experiments showed that while NO number density and NO cooling rate do change with different specifications of the characteristic energy of auroral precipitating electrons, neutral temperature and density recovery remain more or less the same. The reaction rates of key NO chemistry were tested as well, and the NO number density between 110 and 150 km was found to be very sensitive to the reaction rate of $N(^2D) + O_2 \rightarrow NO + O$. A temperature-dependent reaction rate for this reaction proposed by Duff et al. (2003) brought the TIEGCM NO cooling rate at high latitudes closer to the SABER observations. With the temperature-dependent reaction rate, the neutral density recovery time became quite close to the observations in the high-latitude Southern Hemisphere. But model-data discrepancies still exist at low latitudes and in the Northern Hemisphere, which calls for further investigation.

1. Introduction

During geomagnetic storms, a large amount of energy originating from the solar wind and the magnetosphere is dissipated in the coupled ionosphere-thermosphere system, causing significant disturbances in neutral temperature, composition, and density [*Fuller-Rowell et al.*, 1997; *Buonsanto*, 1999]. Measurements from satellite missions, such as the Gravity Field and Steady State Ocean Circulation Explorer (GOCE), CHAllenging Minisatellite Payload (CHAMP), and Gravity Recovery and Climate Experiment (GRACE), along with model studies, have greatly improved our understanding of neutral density variability during geomagnetic storms [e.g., *Forbes et al.*, 2005; *Liu and Lühr*, 2005; *Sutton et al.*, 2005; *Bruinsma et al.*, 2006; *Lei et al.*, 2010, 2011, 2012; *Lu et al.*, 2014]. Simulations are usually capable of capturing the salient features of the storm time thermospheric density variations, but discrepancies with observations still exist [e.g., *Lei et al.*, 2011; *Lu et al.*, 2014]. *Lei et al.* [2011] found that neutral density recovery in Thermosphere-Ionosphere-Electrodynamics General Circulation Model (TIEGCM) simulations was slower than what CHAMP and GRACE had observed during the two superstorms in October 2003. TIEGCM simulations also showed longer relaxation times in the latitude range of 25°N–50°N than at other latitudes. However, relaxation times from observations displayed only a very weak latitudinal dependence. Moreover, the simulated neutral density relaxation time showed a much larger day-night difference compared to observations. *Lu et al.* [2014] performed a Thermosphere-Ionosphere-Mesosphere-Electrodynamics General Circulation Model (TIMEGCM) simulation for the 5 April 2010 geomagnetic storm and compared the simulated neutral density with GOCE, CHAMP, and GRACE observations. Their simulated neutral density recovery times were also longer than those derived from the satellite observations at different altitudes.

The cooling mechanisms in the thermosphere include heat conduction and infrared radiation from CO_2, NO, and O [*Roble*, 1995]. Measurements from the Sounding of the Atmosphere using Broadband Emission

Radiometry (SABER) instrument have provided unprecedented details of CO_2 emission at 15 μm and NO emission at 5.3 μm since 2002 [*Mlynczak et al.*, 2010, 2014; *Hunt et al.*, 2011]. NO emission, which maximizes between 100 and 200 km and mostly occurs at high latitudes, has much larger variations on shorter timescales [*Mlynczak et al.*, 2010] and thus dominates the thermospheric cooling process during geomagnetic storms [*Mlynczak et al.*, 2003, 2005, 2007; *Lu et al.*, 2010]. Utilizing the SABER measurements, *Mlynczak et al.* [2007] showed that the energy radiated by NO accounted for 50% of the total input energy to the upper atmosphere during the geomagnetic storms of April 2002 and suggested NO emission at 5.3 μm to be a natural thermostat for the thermosphere. *Lu et al.* [2010] compared the global Joule heating power from TIEGCM simulations with the global NO cooling power derived from SABER measurements for six selected geomagnetic storms and concluded that, on average, NO infrared emission accounted for about 80% of Joule heating energy input under disturbed conditions. Through cross-correlation analyses, they further pointed out that the global NO radiative power is highly correlated with the 24 h averaged global Joule heating with a time lag of 10 h.

Since NO infrared emission plays the most important role in cooling down the thermosphere during storm times, it is plausible to attribute the slow neutral density recovery to an underestimation of NO cooling in TIEGCM simulations. However, comparisons of NO cooling power between SABER measurements and TIEGCM simulations usually show a fairly good agreement in terms of daily global averages [*Lu et al.*, 2010; *Qian et al.*, 2010; *Burns et al.*, 2012; *Solomon et al.*, 2012]. *Lei et al.* [2011] argued that even though the daily power agrees well, underestimations of NO cooling in TIEGCM simulations may still happen for a particular time interval within a day. Furthermore, the NO cooling rate is a function of NO, O, and neutral temperature [*Kockarts*, 1980], which are all strongly affected by the storm time heating. Therefore, thermospheric recovery is a result of competing heating and cooling processes, each of which may affect the thermospheric recovery following a geomagnetic storm.

The main objective of this study is to assess the key physical processes in the TIEGCM that affect the neutral density recovery during storm periods in light of satellite observations. We also present detailed comparisons of TIEGCM-simulated NO cooling rate with SABER observations. Effects of particle precipitation, which are the main source of NO production at high latitudes during storm times, are examined. The key reaction rates related to NO production are investigated as well and are found to be a very important factor influencing the thermospheric recovery.

2. Data and Model Description

Neutral densities derived from GOCE, CHAMP, and GRACE measurements are utilized in this study to investigate the neutral density recovery during the 5 April 2010 geomagnetic storm. CHAMP was launched on 15 July 2000 into a near-circular orbit at ~450 km with an inclination of 87.3°. Two identical satellites, GRACE-A and GRACE-B, were also launched into high inclination (89.5°), near-circular orbits but at a higher altitude (~500 km) on 17 March 2002. The GOCE satellite was launched on 17 March 2009 and was designed to fly in a 96.7° inclination, near-circular and Sun-synchronous orbit initially at ~270 km. Together, they have provided unprecedented coverage of neutral density measurements, which enables studies of the neutral density variability due to solar, geomagnetic, and low atmospheric wave forcing at different altitudes simultaneously [e.g., *Sutton et al.*, 2006; *Forbes et al.*, 2014; *Lu et al.*, 2014]. During the 5 April 2010 storm period, GOCE, CHAMP, and GRACE were at an average altitude of about 270, 301, and 474 km, respectively. The ascending/descending local time at the orbit's equator crossings was approximately 18:20/06:20 for GOCE, 00:00/12:00 for CHAMP, and 08:45/20:45 for GRACE.

The NO cooling rate inferred from the TIMED/SABER measurements has also been used in this study and compared with the TIEGCM simulations. The TIMED spacecraft was launched in December 2001 into a near-circular orbit at 625 km with an inclination of 74°. The SABER instrument is an infrared radiometer that continuously scans the Earth's limb from a 400 km tangent altitude down to the Earth's surface. It measures infrared radiance (in W m^{-2} sr^{-1}) in 10 distinct spectral channels, one of which is for the NO emission at 5.3 μm. Each measured NO limb radiance profile is inverted to a vertical profile of volume emission rate (in W m^{-3}) by applying an Abel inversion and assuming that the NO emission is in the weak-line radiative transfer limit [*Mlynczak et al.*, 2010; *Hunt et al.*, 2011]. In addition, an adjustment factor is applied to the volume emission rate to account for the NO emission outside the instrument bandpass. The radiative flux (in W m^{-2}) can be obtained by integrating the volume emission rate profile vertically from 100 to 250 km, and the total radiative power is then

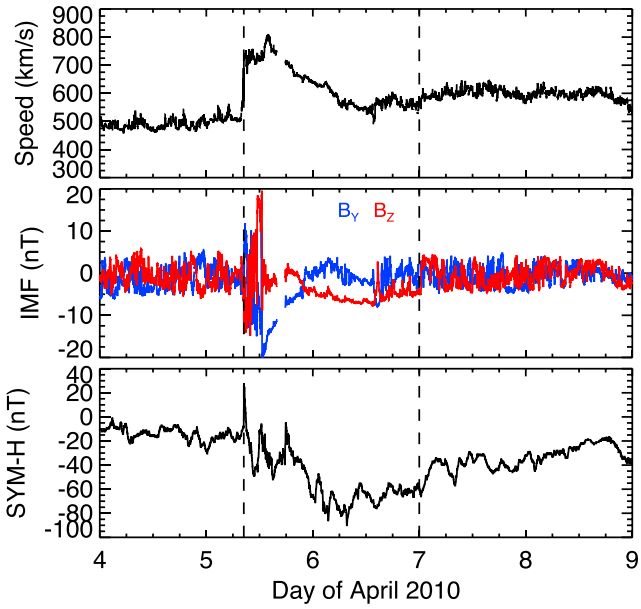

Figure 1. (top) One minute temporal resolution solar wind speed, (middle) the IMF B_Y and B_Z components, and (bottom) *SYM-H* index from 5 to 8 April 2010. The first vertical dashed line marks the onset of the storm at 08:27 UT on 5 April. The second vertical dashed line marks the start of the thermospheric recovery phase at 00:00 UT on 7 April.

estimated by integrating the flux with respect to the area. SABER provided NO cooling rate at local times of about 0600 and 2100 h during the studied period, covering the latitude range from ~83°S to ~55°N.

The National Center for Atmospheric Research (NCAR) TIEGCM is a time-dependent, three-dimensional model of the coupled thermosphere and ionosphere system, which solves the fully coupled, nonlinear, hydrodynamic, thermodynamic, and continuity equations of the neutral gas self-consistently with the ion energy, ion momentum, and ion continuity equations [*Roble et al.*, 1988; *Richmond et al.*, 1992]. For this study, we use the high-resolution version of the TIEGCM, which has a horizontal resolution of 2.5° × 2.5° in longitude and latitude and a vertical resolution of a quarter scale height. Input parameters for the model include solar extremely ultraviolet and ultraviolet fluxes, which are parameterized by the $F_{10.7}$ index, high-latitude particle precipitation, and convection electric fields. The latter two are specified by the assimilative mapping of the ionospheric electrodynamics (AMIE) [*Richmond and Kamide*, 1988] outputs in this study. More details regarding the observational data used to generate the AMIE outputs for this particular event can be found in *Lu et al.* [2014]. At the lower boundary, the model is driven by the global scale wave model [*Hagan and Forbes*, 2002], including migrating diurnal and semidiurnal tides.

3. Results and Discussion

3.1. TIEGCM Simulations of the 5 April 2010 Geomagnetic Storm

Figure 1 shows the 1 min temporal resolution solar wind speed, interplanetary magnetic field (IMF) B_Y and B_Z components, and the *SYM-H* index during the period of 4–8 April 2010. An interplanetary coronal mass injection (ICME), with a maximum solar wind speed of ~800 km s^{-1}, arrived at the Earth on 5 April 2010 and triggered a geomagnetic storm around 08:27 UT as marked by the first vertical dashed line in Figure 1 [*McComas et al.*, 2012; *Lu et al.*, 2014]. The *SYM-H* index reached a minimum of −90 nT on 6 April 2010. The second vertical dashed line depicts the beginning of the thermospheric recovery phase at 00:00 UT on 7 April 2010, and thereafter, the IMF returned to its pre-ICME condition and the Joule heating energy dissipation in the thermosphere subsided [*Lu et al.*, 2014]. The ionospheric and thermospheric response to this storm event has been studied by *Lu et al.* [2014] using the TIMEGCM model and measurements from the GOCE, CHAMP, and GRACE satellites. One interesting result they found is that the simulated recovery times of neutral density were ~6 h longer than those derived from GOCE, CHAMP, and GRACE observations. A longer relaxation time in the simulated neutral density has also been reported by *Lei et al.* [2011], in which the TIEGCM model was used to simulate the Halloween storm of October 2003, and the simulation results were compared with CHAMP and GRACE measurements. While thermospheric recovery may vary among different storms, the neutral density recovery in TIMEGCM/TIEGCM simulations is usually slower than what observations indicate. In this study we apply the TIEGCM model to simulate the 5 April 2010 storm, with an aim to determine the key factors controlling the thermospheric recovery after the storm.

Percentage changes of global mean neutral temperature and density from the TIEGCM simulations at several selected altitudes (100, 150, 250, 300, and 475 km) are shown in Figures 2a and 2b, respectively. Data on 4 April 2010 are chosen as a reference to calculate the percentage change. On average, global mean temperature increases by about 8% at 150 km and by about 13% at higher altitudes during the storm time.

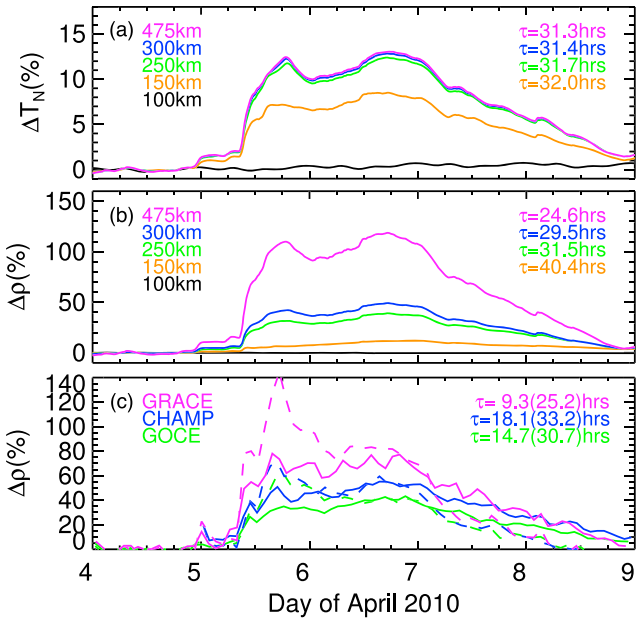

Figure 2. (a) Percentage change of TIEGCM global mean neutral temperature at selected heights, (b) percentage change of TIEGCM global mean neutral density at selected heights, and (c) percentage change of orbit-mean neutral density along GOCE (green), CHAMP (blue), and GRACE (magenta) trajectories, with observations shown by dashed lines and TIEGCM simulation results by solid lines. The parameter τ denotes the *e*-folding recovery time. In Figure 2c, the value outside (inside) the parenthesis is from observations (simulations).

The increase in global mean neutral density ranges from ~10% at 100 km to ~120% at 475 km. Comparisons of orbit-mean neutral density along satellite trajectories between observations (dashed) and simulations (solid) are shown in Figure 2c. Simulations are able to capture the salient features of the neutral density variations observed by GOCE, CHAMP, and GRACE satellites, but with smaller peaks during the main phase and longer tails during the recovery phase. The τ in Figure 2 denotes the *e*-folding recovery time, which represents the time interval when the neutral density drops from ρ_0 (neutral density at the beginning of the thermospheric recovery) to ρ_0/e. Global mean temperature takes ~31 h to recover at the selected altitudes. The recovery times of global mean neutral density are on the same order and generally shorter than those of the global mean temperature above 150 km. In Figure 2c, the marked recovery times outside (inside) the parentheses are from measurements (simulations). Neutral density recovery times from simulations are longer than those from GOCE, CHAMP, and GRACE observations, which are similar to what has been noted in *Lei et al.* [2011] and *Lu et al.* [2014].

Since NO infrared emission is the most important cooling mechanism during storm periods, including the recovery phase [*Mlynczak et al.*, 2007; *Lu et al.*, 2010], it is possible that the slow thermospheric recovery in TIEGCM simulations is due to the underestimation of NO cooling in the model. To validate that, we compare the NO cooling rate simulated by TIEGCM with the SABER measurements along the TIMED satellite trajectory, and the results are shown in Figure 3. NO cooling power (in W) is plotted against UT and latitude for 4–7 April 2010. The SABER measurements are shown in Figure 3 (left column) and the TIEGCM simulations in Figure 3 (right column). SABER was in the "southward" viewing mode during this storm period and sampled the thermosphere from ~83°S to ~55°N. As a result, there were no observations for the high-latitude Northern Hemisphere. Overall, TIEGCM is doing a fairly good job in reproducing NO cooling power. The SABER measurements show that NO cooling power maximized at high latitudes, with large increases during the storm main and recovery phases on 6 and 7 April. These salient features have been successfully simulated by TIEGCM, though some quantitative differences can be easily identified. For example, the TIEGCM simulated NO cooling power at high latitudes is smaller than that from the SABER measurements. In addition, TIEGCM seemed to overestimate NO cooling power at low latitudes and the strong tidal signatures in the TIEGCM-simulated NO cooling power at low latitudes can be seen only barely in the SABER measurements. We suspect that the overestimation at low latitudes and the underestimation at high latitudes may have resulted in the fact that the daily average of NO cooling power from the TIEGCM simulations agrees well with SABER measurements [*Lu et al.*, 2010; *Qian et al.*, 2010]. It is reasonable to anticipate that the thermospheric recovery in the TIEGCM simulations would be more realistic and closer to observations with more accurate modeling of the NO cooling rate, especially a larger NO cooling rate at high latitudes during storm periods.

The NO cooling rate (erg cm^{-3} s^{-1}) in the standard version of the TIEGCM is calculated based on *Kockarts* [1980] as follows:

$$\text{NO Cooling Rate} = \frac{h\nu_0 A_{10}\, n(\text{NO}_{v=0}) \times (k_{\text{O}}\, n(\text{O}) + k_{\text{O}_2}\, n(\text{O}_2))}{k_{\text{O}}\, n(\text{O}) + k_{\text{O}_2}\, n(\text{O}_2) + A_{10}} \times e^{-\frac{h\nu_0}{k_B T_N}}, \quad (1)$$

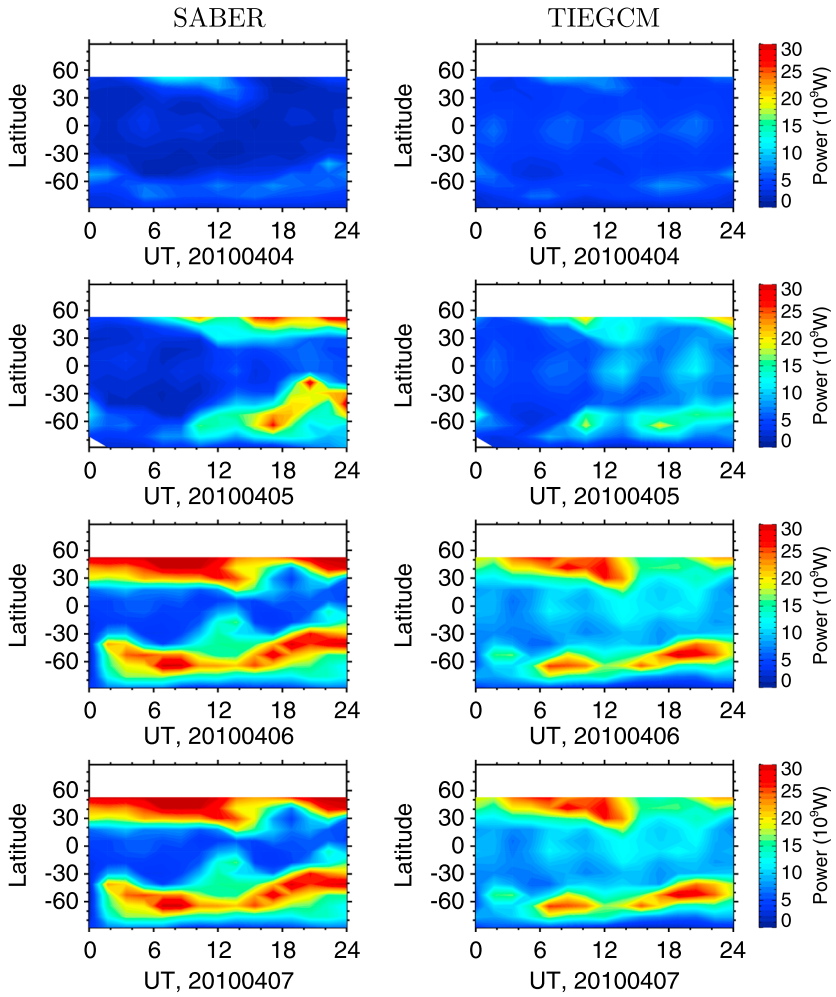

Figure 3. NO cooling power along TIMED trajectory from (left column) SABER measurements and (right column) TIEGCM simulations. The SABER instrument is in the "southward" viewing mode, so there are no observations beyond ~55°N.

where h is Planck's constant, $\nu_0 = c/\lambda 0$, $\lambda 0 = 5.3$ μm, A_{10} is the transition probability of NO($v=1$) → NO($v=0$) + $h\nu_0$, which is equal to 13.3 s^{-1}, $n(NO_{v=0})$, $n(O)$, and $n(O_2)$ are number densities of NO($v=0$), O, and O_2, respectively, k_O is the vibrational relaxation rate of NO($v=1$) by collisions with O (NO($v=1$) + O $\xrightarrow{k_O}$ NO($v=0$) + O), which is set to be 4.2×10^{-11} cm^3 s^{-1} [*Hwang et al.*, 2003], k_{O_2} is the vibrational relaxation rate of NO ($v = 1$) by collisions with O_2, which is set to be 2.4×10^{-14} cm^3 s^{-1} [*Murphy et al.*, 1975], k_B is Boltzmann's constant, and T_N is neutral temperature. With this equation, the NO 5.3 μm emission is assumed to be in the weak-line radiative transfer limit, which has been confirmed in *Mlynczak et al.* [2005]. NO number density is the focus of this study, as it is believed to be one of the primary causes of NO cooling increase at high latitudes during storm times [*Mlynczak et al.*, 2005]. In the following sections, several factors that control the NO production are examined, and their further effects on the NO cooling rate and the overall thermospheric recovery are discussed.

3.2. Effects of Particle Precipitation

Solar radiation, which causes the ionization, dissociation, and excitation of N2, is the main source for daytime NO production [*Barth et al.*, 1988, 1999]. Particle precipitation is another prominent source at high latitudes, especially during disturbed times [*Gerard and Barth*, 1977; *Solomon et al.*, 1999]. Since the storm time NO cooling power at high latitudes in the TIEGCM simulations is found to be smaller than SABER measurements, a modified TIEGCM run (hereafter M1, see Table 1), with the total energy flux of auroral electron precipitation doubled and the characteristic energy unchanged, is conducted. Here we assume that the auroral electron

Table 1. Descriptions of Different Test Runs

Test Run	Differences From the Standard Run
M1	Energy flux of auroral electron precipitation × 2
M2	Same energy flux, but characteristic energy × 1.5
M3	Same energy flux, but characteristic energy × 0.5
M4	With the reaction rate from *Duff et al.* [2003]

energy flux obtained from AMIE has underestimated the true auroral flux by a factor of 2, with the expectation that the modified model run would increase the storm time NO production at high latitudes as well as the NO cooling rate.

Figure 4 (first row) compares the ionization rate due to auroral electron precipitation (QAURORA), neutral temperature, NO number density, and NO cooling rate at 71.25°N at midnight (00:00 LT) between a standard TIEGCM run (solid) and M1 (dashed). This location is chosen since it is inside the auroral zone. We also took a look at the comparisons at other auroral locations away from local midnight, and the main findings are similar to what we describe below. Profiles from both quiescent (12:00 UT on 4 April, black lines) and disturbed (12:00 UT on 6 April, red lines) times are plotted out. Since we only double the energy flux during the storm time, the black solid and dashed lines are overlapping with each other in each plot. First of all, by comparing the solid black lines with the solid red ones, we can see that all the parameters shown have increased significantly during the storm time, which demonstrates the strong impact of the geomagnetic storm on the coupled thermosphere-ionosphere system. For example, the neutral temperature at 300 km increases by ~120 K and the peak NO cooling rate increases from 1.0×10^{-8} to 3.4×10^{-8} W m^{-3}. When the precipitating electron flux is doubled (shown by the red dashed lines), the ionization rate is nearly doubled at all altitudes compared with the standard run (shown by the red solid lines), with its maximum value changing from ~3.4×10^4 to ~6.8×10^4 cm^{-3} s^{-1}. Neutral temperature increases at all altitudes above ~120 km and by ~35 K at 300 km. Similar to the ionization rate, NO number density increases at all altitudes as well, and its peak density is enhanced by ~1.5 times (from 2.8×10^8 to 4.1×10^8 cm^{-3}). The most significant change in the NO cooling rate takes place between 100 and 200 km where the cooling rate maximizes. The NO cooling rate largely increases in this region as a result of the enhancements in both temperature and NO number density. O number density displays only minor variations when doubling the auroral energy flux (not shown). The maximum NO cooling rate is also increased by ~1.5 times (from 3.4×10^{-8} to 4.8×10^{-8} W m^{-3}). The additional cooling does bring down the recovery times of global mean neutral temperature, global mean neutral density, and orbit-mean neutral density along satellite trajectories by ~4–9 h as shown in Figure S1 in the supporting information. However, the additional particle precipitation largely increases ionospheric conductivity and causes significant enhancements in Joule heating. As a result, the simulated percentage increases in orbit-mean neutral density are larger than those derived from the satellite measurements by a factor of ~2 during the storm main phase on 6 April. We therefore do not think that the simulation results from M1 are realistic.

From the simulation results of M1, it is noted that the peaks of NO number density and NO cooling rate locate at different altitudes. NO number density peaks around 105 km, but NO cooling rate maximizes approximately at 125 km. If only NO number density was responsible for the underestimation of NO cooling, more NO is required between 110 and 150 km. We also notice that the increase in NO number density during the storm time is roughly proportional to the ionization rate due to auroral particle precipitation. Particles with different energies penetrate to different altitudes [*Millward et al.*, 1999; *Fang et al.*, 2008], and thus, by modifying the characteristic energy of precipitating particles, the ionization profiles may vary and NO production may change accordingly. To understand how the characteristic energy of auroral electron precipitation affects the NO number density and the NO cooling rate, we perform another two test runs. In both runs, the total energy flux of auroral electron precipitation is kept the same, but the characteristic energy is increased by 1.5 in one run (hereafter M2) and decreased by 0.5 in the other run (hereafter M3).

The ionization rate, neutral temperature, NO number density, and NO cooling rate at 71.25°N at midnight from M2 and M3 are compared with those from the standard TIEGCM run in Figures 4 (third row) and 4 (fourth row), respectively. By increasing the characteristic energy of precipitating electrons, the ionization peak moves down to a lower altitude. Comparing to the profile from the standard run, the ionization rate becomes larger

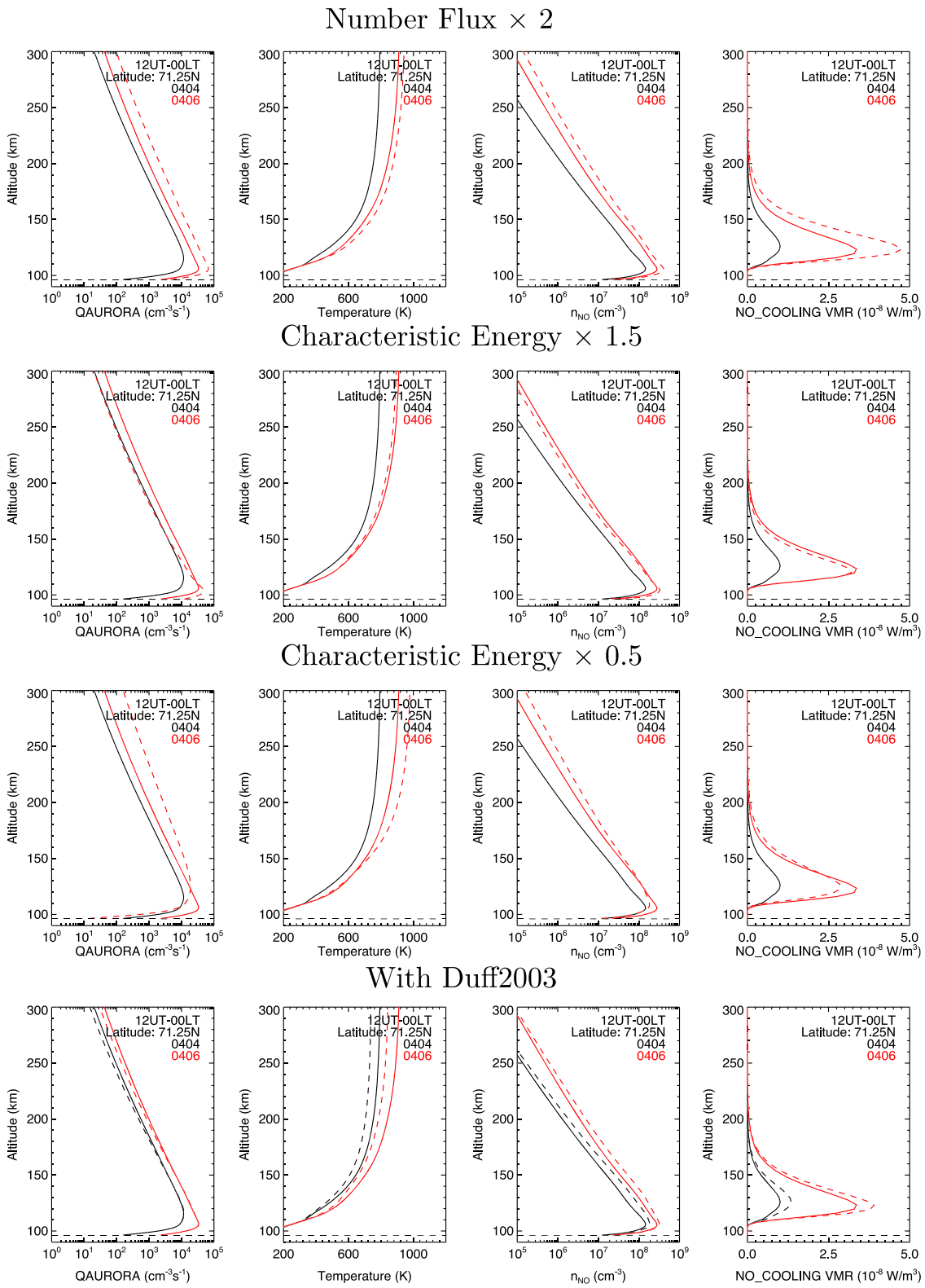

Figure 4. Comparisons of the ionization rate (QAURORA) due to particle precipitation, neutral temperature, NO number density, and NO cooling rate at 71.25°N at midnight (00:00 LT) between a standard TIEGCM run and a modified run. Profiles on the quiet day (12:00 UT on April 4) are plotted out in black, and profiles on the storm day (12:00 UT on 6 April) in red. Profiles from the standard TIEGCM run are plotted using solid lines and are unchanged between rows, while the row-dependent profiles from each modified run are plotted using dashed lines. From top to bottom, it shows the comparisons between the standard TIEGCM run with (first row) M1, (second row) M2, (third row) M3, and (fourth row) M4.

below ~110 km and smaller at higher altitudes. In contrast, by decreasing the characteristic energy, the ionization peak moves up to a higher altitude, and the ionization rate decreases (increases) below (above) ~120 km compared to the standard run. NO production changes accordingly, roughly following the variations of the ionization rates as mentioned earlier. However, in both cases, the most distinct change in NO number density can be found either above 150 km or below 110 km and the NO number density between 110 and 150 km is only slightly affected. Neutral temperature exhibits interesting response too. Temperature decreases by ~20 K above 200 km when increasing the characteristic energy by 1.5 times and increases by ~60 K when reducing the characteristic energy by one half of its original value. Similarly, the temperature variations between 110 and 150 km are almost negligible. As a result, the NO cooling rate becomes somewhat smaller above its peak altitude in M2. At the same time, it decreases around the peak altitude and increases between 140 and 200 km in M3. Overall, NO cooling does not change much in both cases, which suggests that the NO cooling rate is not very sensitive to the characteristic energy of auroral precipitating electrons. Consequently, neutral temperature and density recovery remain more or less the same as shown in Figures S2 and S3 in the supporting information.

3.3. Reaction Rates of Key NO Chemistry

The reactions listed below are the key chemical processes related to the NO production and loss in the upper atmosphere:

$$N(^4S) + O_2 \rightarrow NO + O, \quad \text{(R1)}$$

$$N(^2D) + O_2 \rightarrow NO + O, \quad \text{(R2)}$$

$$N(^4S) + NO \rightarrow N_2 + O, \quad \text{(R3)}$$

$$NO + h\nu \rightarrow N(^4S) + O, \quad \text{(R4)}$$

$$N(^2D) + O \rightarrow N(^4S) + O. \quad \text{(R5)}$$

The NO production comes from the reactions between atomic nitrogen and molecular oxygen (R1 and R2). $N(^4S)$ is the ground state of atomic nitrogen, and $N(^2D)$ is the first excited state, which can be deactivated to $N(^4S)$ through collisions with O (reaction (R5)). Reaction (R1) is highly temperature dependent and dominates the NO production at higher altitudes when the temperature is high enough. Reaction (R2), on the other hand, is the most important NO source around the peak altitude (~110 km). Reaction (R3) destroys $N(^4S)$ and NO at the same time. Photodissociation of NO by solar far ultraviolet radiation (R4), which is parameterized by TIEGCM based on $F_{10.7}$ according to *Minschwaner and Siskind* [1993], provides another loss mechanism for NO.

As reviewed by *Yonker* [2013], large uncertainties exist in the reaction rates of key NO chemistry and there have been many updates to these rates in the last decade either theoretically or experimentally. These updates are yet to be applied in TIEGCM. Different studies usually give rise to different reaction rates, and many experiments are conducted under the conditions when the temperature is below 400–600 K, which makes it more difficult to find appropriate reaction rates for upper atmosphere modeling where temperature goes beyond 600 K. It also requires a considerable amount of efforts to adopt new reaction rates while maintaining the internal stability and consistency of the model. We briefly tested those latest reaction rates summarized in *Yonker* [2013] and *Yonker et al.* [2014] and found that NO number density increases noticeably at all altitudes after applying the temperature-dependent reaction rate ($6.2 \times 10^{-12}(T/300)$ cm^3 s^{-1}) proposed by *Duff et al.* [2003] for reaction (R2). Note that TIEGCM has been using a fixed rate (5.0×10^{-12} cm^3 s^{-1}) for this reaction as default. Figure 5 indicates that with the reaction rate (the red line) from *Duff et al.* [2003], the NO production from reaction (R2) is larger than the model's default value (the black line) when the temperature is above ~245 K. When the temperature reaches 500 K, the Duff production rate is nearly twice the default value.

Another test run (hereafter M4) was performed with the reaction rate from *Duff et al.* [2003]. Figure 4 (fourth row) shows the comparisons of the ionization rate due to particle precipitation, neutral temperature, NO number density, and NO cooling rate at 71.25°N at midnight between M4 and the standard run. Temperature profiles indicate that in the critical NO cooling region of 100–150 km the neutral temperature ranges from ~200 to ~600 K during the quiet time and becomes even larger during the storm time. Therefore, the Duff reaction rate can significantly increase the NO production in this altitudinal range. When the new reaction

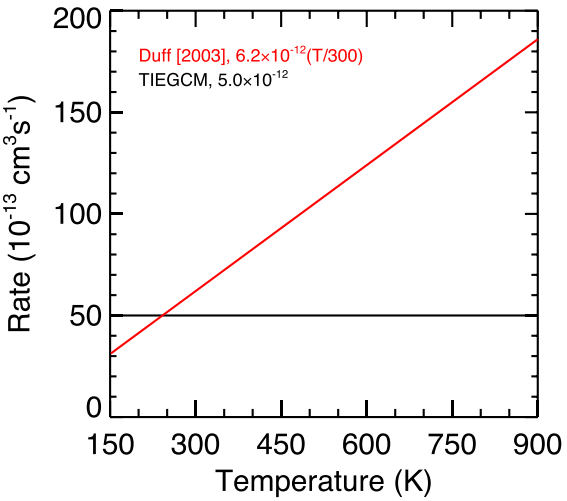

Figure 5. Reaction rates for the $N(^2D) + O_2 \rightarrow NO + O$ reaction used in TIEGCM (black) and proposed by *Duff et al.* [2003] (red).

rate is applied, NO density increases at all altitudes during both quiet and disturbed times, so do the NO cooling rate but mainly between 110 and 150 km. The NO cooling rate maximum increases from 1.0×10^{-8} to 1.4×10^{-8} W m^{-3} during the quiet time and from 3.4×10^{-8} to 3.9×10^{-8} W m^{-3} on the storm day. Temperature decreases above 110 km altitude in response to the additional cooling, by ~60 and ~75 K at 300 km on the quiet and storm days, respectively. The decrease in temperature reduces the scale height and thus reduces the neutral density at higher altitudes. Consequently, the ionization rate is slightly decreased above 150 km.

Figure 6 shows the daily zonal mean NO cooling power, with the SABER measurements in solid black, the simulated power from the standard TIEGCM run in dashed black, and from M4 in dashed red. With the reaction rate from *Duff et al.* [2003], the simulated NO cooling power is brought closer to measurements at high latitudes, especially in the Southern Hemisphere. But there is still an underestimation in the Northern Hemisphere. In addition, the new reaction rate does not improve the discrepancy at low latitudes, which needs further investigation in future studies.

Percentage changes of global mean neutral temperature, global mean neutral density, and orbit-mean density along satellite trajectories from M4 are plotted out in Figure 7 from 4 to 8 April. Since the upper boundary altitude of M4 sometimes falls below 475 km due to the large cooling effect introduced by the Duff reaction rate, global mean neutral temperature and density at 475 km and orbital mean neutral density along the GRACE trajectories from M4 are obtained through extrapolation in order to make Figure 7 conform to Figure 2. The temperature-dependent reaction rate reduces the recovery time of global mean neutral temperature by ~7 h at all altitudes. The recovery time of global mean neutral density also decreases by ~3 to ~8 h, depending on altitude. Furthermore, the relaxation times of orbit-mean neutral density along satellite trajectories are all decreased, though still larger than those derived from the satellite measurements. Since the simulated NO cooling power at high latitudes is now in a better agreement with the SABER measurements, we break down the orbit-mean neutral density to three latitudinal regions: (1) the middle to high latitudes in the Northern Hemisphere from 30°N to 90°N, (2) the low latitudes from 30°S to 30°N, and (3) the middle to high latitudes in the Southern Hemisphere from 30°S to 90°S. Comparisons of mean neutral density in the different latitudinal regions are shown in Figure 8. The satellite measurements (dashed lines) are compared with the simulation

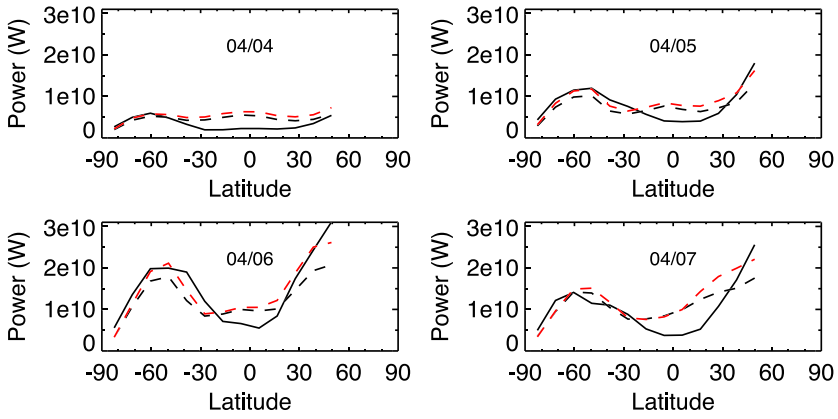

Figure 6. Daily zonal mean NO cooling power from SABER measurements (solid black), the standard TIEGCM run (dashed black) and the modified run with reaction rate from *Duff et al.* [2003] (red dashed).

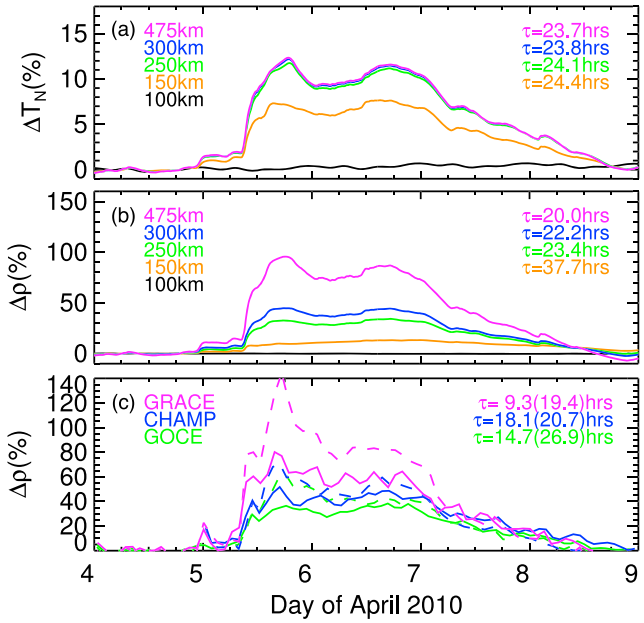

Figure 7. Same as Figure 2 but for the modified TIEGCM run (M4) with the reaction rate from *Duff et al.* [2003].

results (solid lines) from the standard TIEGCM run on the left, and with those from M4 on the right. Figure 8 indicates that neutral density recovery becomes faster at all satellite altitudes and at all latitudes with the reaction rate from *Duff et al.* [2003]. Furthermore, the neutral density recovery times at middle to high latitudes in the Southern Hemisphere become quite close to those derived from the satellite measurements, with a maximum difference of 1.4 h. The simulated recovery times at low latitudes and in the Northern Hemisphere are still ~3 to ~14 h longer. Had the underestimation of NO cooling in the high-latitude Northern Hemisphere been fixed, we anticipate that the neutral density recovery would be more realistic at all latitudes. In follow-on

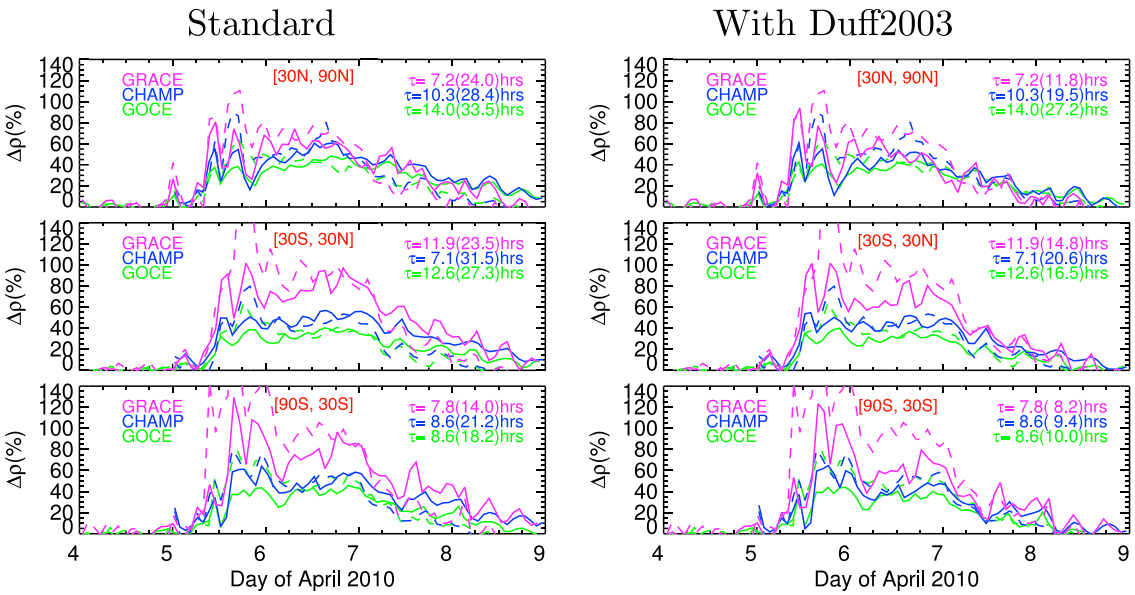

Figure 8. Percentage changes of orbit-mean neutral density along GOCE (green), CHAMP (blue), and GRACE (magenta) trajectories in the latitudinal regions of (top row) 30°N–90°N, (middle row) 30°S–30°N, and (bottom row) 30°S–90°S. Observations are shown by dashed lines and simulations by solid lines. Comparisons between observations and the standard TIEGCM run are shown on the left, and comparisons between observations and the modified run with the reaction rate (M4) from *Duff et al.* [2003] on the right. The parameter τ denotes the *e*-folding recovery time, with the value outside (inside) the parenthesis being derived from observations (simulations).

studies, we plan to further explore the causes of the remaining model data discrepancies in the northern high-latitude region as well as at low latitudes.

4. Summary

Thermospheric recovery during the 5 April 2010 geomagnetic storm has been investigated in this paper by utilizing TIEGCM and the neutral density measurements from the GOCE, CHAMP, and GRACE satellites. It was found that the simulated neutral density recovery was much slower than the observations had indicated. We further compared the NO cooling rate from the TIEGCM simulations with TIMED/SABER measurements, which revealed underestimations of NO cooling power at high latitudes in both hemispheres and overestimations at low latitudes. Modifying the specifications (namely, the characteristic energy and the number flux) of particle precipitation did not help accelerate the thermospheric cooling process. When the temperature-dependent reaction rate from *Duff et al.* [2003] was adopted for the reaction between $N(^2D)$ and O_2, NO number density at high latitudes increased at all altitudes, so was the NO cooling rate between 110 and 150 km. The temperature-dependent reaction rate brought the simulated NO cooling power closer to SABER measurements although discrepancies still existed at low latitudes and in the Northern Hemisphere. The additional NO cooling accelerated the neutral density recovery at all altitudes and latitudes, especially at middle to high latitudes in the Southern Hemisphere, where the maximum difference between the recovery times derived from the simulations and observations were only 1.4 h. Neutral density recovery at low latitudes and in the Northern Hemisphere remained quite slow compared with observations, which needs further investigation.

Acknowledgments

This work was supported by the U.S. Participating Investigator (USPI) program under National Aeronautics and Space Administration (NASA) grant NNX12AD26G. We acknowledge the OMNIWeb service (http://omniweb.gsfc.nasa.gov/) at NASA/Goddard Space Flight Center (GSFC) for providing SW/IMF conditions and *SYM-H* index. We also acknowledge the German Space Operations Center (GSOC) of the German Aerospace Center (DLR) for providing GRACE data, GFZ Helmholtz Center Potsdam for providing CHAMP data, and European Space Agency (ESA) for providing GOCE data. SABER-measured NO cooling data can be accessed from http://saber.gats-inc.com/browse_data.php. We would like to acknowledge high-performance computing support from Yellowstone provided by NCAR's Computational and Information Systems Laboratory and sponsored by National Science Foundation (NSF). The TIEGCM simulations and AMIE outputs used in this study are archived on NCAR's High Performance Storage System and are available on request. Gang Lu was supported in part by the NASA Living With a Star (LWS) program under grant NNX14AE08G. Wenbin Wang was supported in part by the NASA LWS program under grants NNX14AE06G and NNX15AB83G. NCAR is sponsored by the NSF.

References

Barth, C. A., W. K. Tobiska, D. E. Siskind, and D. D. Cleary (1988), Solar-terrestrial coupling—Low-latitude thermospheric nitric oxide, *Geophys. Res. Lett.*, *15*, 92–94, doi:10.1029/GL015i001p00092.

Barth, C. A., S. M. Bailey, and S. C. Solomon (1999), Solar-terrestrial coupling: Solar soft X-rays and thermospheric nitric oxide, *Geophys. Res. Lett.*, *26*, 1251–1254, doi:10.1029/1999GL900237.

Bruinsma, S., J. M. Forbes, R. S. Nerem, and X. Zhang (2006), Thermosphere density response to the 20–21 November 2003 solar and geomagnetic storm from CHAMP and GRACE accelerometer data, *J. Geophys. Res.*, *111*, A06303, doi:10.1029/2005JA011284.

Buonsanto, M. J. (1999), Ionospheric storms—A review, *Space Sci. Rev.*, *88*, 563–601, doi:10.1023/A:1005107532631.

Burns, A. G., S. C. Solomon, L. Qian, W. Wang, B. A. Emery, M. Wiltberger, and D. R. Weimer (2012), The effects of corotating interaction region/high speed stream storms on the thermosphere and ionosphere during the last solar minimum, *J. Atmos. Sol. Terr. Phys.*, *83*, 79–87, doi:10.1016/j.jastp.2012.02.006.

Duff, J. W., H. Dothe, and R. D. Sharma (2003), On the rate coefficient of the $N(^2D) + O_2 \rightarrow NO + O$ reaction in the terrestrial thermosphere, *Geophys. Res. Lett.*, *30*(5), 1259, doi:10.1029/2002GL016720.

Fang, X., C. E. Randall, D. Lummerzheim, S. C. Solomon, M. J. Mills, D. R. Marsh, C. H. Jackman, W. Wang, and G. Lu (2008), Electron impact ionization: A new parameterization for 100 eV to 1 MeV electrons, *J. Geophys. Res.*, *113*, A09311, doi:10.1029/2008JA013384.

Forbes, J., J. Zhang, E. Doornbos, S. Bruinsma, X. Zhang, and C. Zhang (2014), Lunar tide variability in thermosphere density as derived from GOCE, CHAMP and GRACE accelerometer data, *Geophys. Res. Abstr.*, vol. 16, EGU2014-2459 presented at 2014 EGU General Assembly, Vienna, Austria, 27 Apr–2 May.

Forbes, J. M., G. Lu, S. Bruinsma, S. Nerem, and X. Zhang (2005), Thermosphere density variations due to the 15–24 April 2002 solar events from CHAMP/STAR accelerometer measurements, *J. Geophys. Res.*, *110*, A12S27, doi:10.1029/2004JA010856.

Fuller-Rowell, T. J., M. V. Codrescu, R. G. Roble, and A. D. Richmond (1997), How does the thermosphere and ionosphere react to a geomagnetic storm?, in *Magnetic Storms, Geophys. Monogr. Ser.*, vol. 98, edited by B. T. Tsurutani et al., pp. 203–225, AGU, Washington, D. C., doi:10.1029/GM098p0203.

Gerard, J.-C., and C. A. Barth (1977), High-latitude nitric oxide in the lower thermosphere, *J. Geophys. Res.*, *82*, 674–680, doi:10.1029/JA082i004p00674.

Hagan, M. E., and J. M. Forbes (2002), Migrating and nonmigrating diurnal tides in the middle and upper atmosphere excited by tropospheric latent heat release, *J. Geophys. Res.*, *107*(D24), 4754, doi:10.1029/2001JD001236.

Hunt, L. A., M. G. Mlynczak, B. T. Marshall, C. J. Mertens, J. C. Mast, R. E. Thompson, L. L. Gordley, and J. M. Russell III (2011), Infrared radiation in the thermosphere at the onset of solar cycle 24, *Geophys. Res. Lett.*, *38*, L15802, doi:10.1029/2011GL048061.

Hwang, E. S., K. J. Castle, and J. A. Dodd (2003), Vibrational relaxation of NO($v = 1$) by oxygen atoms between 295 and 825 K, *J. Geophys. Res.*, *108*(A3), 1109, doi:10.1029/2002JA009688.

Kockarts, G. (1980), Nitric oxide cooling in the terrestrial thermosphere, *Geophys. Res. Lett.*, *7*, 137–140, doi:10.1029/GL007i002p00137.

Lei, J., J. P. Thayer, A. G. Burns, G. Lu, and Y. Deng (2010), Wind and temperature effects on thermosphere mass density response to the November 2004 geomagnetic storm, *J. Geophys. Res.*, *115*, A05303, doi:10.1029/2009JA014754.

Lei, J., J. P. Thayer, G. Lu, A. G. Burns, W. Wang, E. K. Sutton, and B. A. Emery (2011), Rapid recovery of thermosphere density during the October 2003 geomagnetic storms, *J. Geophys. Res.*, *116*, A03306, doi:10.1029/2010JA016164.

Lei, J., A. G. Burns, J. P. Thayer, W. Wang, M. G. Mlynczak, L. A. Hunt, X. Dou, and E. Sutton (2012), Overcooling in the upper thermosphere during the recovery phase of the 2003 October storms, *J. Geophys. Res.*, *117*, A03314, doi:10.1029/2011JA016994.

Liu, H., and H. Lühr (2005), Strong disturbance of the upper thermospheric density due to magnetic storms: CHAMP observations, *J. Geophys. Res.*, *110*, A09S29, doi:10.1029/2004JA010908.

Lu, G., M. G. Mlynczak, L. A. Hunt, T. N. Woods, and R. G. Roble (2010), On the relationship of Joule heating and nitric oxide radiative cooling in the thermosphere, *J. Geophys. Res.*, *115*, A05306, doi:10.1029/2009JA014662.

Lu, G., M. E. Hagan, K. Häusler, E. Doornbos, S. Bruinsma, B. J. Anderson, and H. Korth (2014), Global ionospheric and thermospheric response to the 5 April 2010 geomagnetic storm: An integrated data-model investigation, *J. Geophys. Res. Space Physics*, *119*, 10,358–10,375, doi:10.1002/2014JA020555.

McComas, D. J., N. Buzulukova, M. G. Connors, M. A. Dayeh, J. Goldstein, H. O. Funsten, S. Fuselier, N. A. Schwadron, and P. Valek (2012), Two wide-angle imaging neutral-atom spectrometers and interstellar boundary explorer energetic neutral atom imaging of the 5 April 2010 substorm, *J. Geophys. Res.*, *117*, A03225, doi:10.1029/2011JA017273.

Millward, G. H., R. J. Moffett, H. F. Balmforth, and A. S. Rodger (1999), Modeling the ionospheric effects of ion and electron precipitation in the cusp, *J. Geophys. Res.*, *104*, 24,603–24,612, doi:10.1029/1999JA900249.

Minschwaner, K., and D. E. Siskind (1993), A new calculation of nitric oxide photolysis in the stratosphere, mesosphere, and lower thermosphere, *J. Geophys. Res.*, *98*, 20,401–20,412, doi:10.1029/93JD02007.

Mlynczak, M., et al. (2003), The natural thermostat of nitric oxide emission at 5.3 µm in the thermosphere observed during the solar storms of April 2002, *Geophys. Res. Lett.*, *30*(21), 2100, doi:10.1029/2003GL017693.

Mlynczak, M. G., et al. (2005), Energy transport in the thermosphere during the solar storms of April 2002, *J. Geophys. Res.*, *110*, A12S25, doi:10.1029/2005JA011141.

Mlynczak, M. G., F. J. Martin-Torres, and J. M. Russell (2007), Correction to "Energy transport in the thermosphere during the solar storms of April 2002", *J. Geophys. Res.*, *112*, A02303, doi:10.1029/2006JA012008.

Mlynczak, M. G., et al. (2010), Observations of infrared radiative cooling in the thermosphere on daily to multiyear timescales from the TIMED/SABER instrument, *J. Geophys. Res.*, *115*, A03309, doi:10.1029/2009JA014713.

Mlynczak, M. G., L. A. Hunt, C. J. Mertens, B. Thomas Marshall, J. M. Russell, T. Woods, R. Earl Thompson, and L. L. Gordley (2014), Influence of solar variability on the infrared radiative cooling of the thermosphere from 2002 to 2014, *Geophys. Res. Lett.*, *41*, 2508–2513, doi:10.1002/2014GL059556.

Murphy, R. E., E. T. P. Lee, and A. M. Hart (1975), Quenching of vibrationally excited nitric oxide by molecular oxygen and nitrogen, *J. Chem. Phys.*, *63*, 2919–2925, doi:10.1063/1.431701.

Qian, L., S. C. Solomon, and M. G. Mlynczak (2010), Model simulation of thermospheric response to recurrent geomagnetic forcing, *J. Geophys. Res.*, *115*, A10301, doi:10.1029/2010JA015309.

Richmond, A. D., and Y. Kamide (1988), Mapping electrodynamic features of the high-latitude ionosphere from localized observations—Technique, *J. Geophys. Res.*, *93*, 5741–5759, doi:10.1029/JA093iA06p05741.

Richmond, A. D., E. C. Ridley, and R. G. Roble (1992), A thermosphere/ionosphere general circulation model with coupled electrodynamics, *Geophys. Res. Lett.*, *19*, 601–604, doi:10.1029/92GL00401.

Roble, R. G. (1995), Energetics of the mesosphere and thermosphere, in *The Upper Mesosphere and Lower Thermosphere: A Review of Experiment and Theory, Geophys. Monogr. Ser.*, vol. 87, edited by R. M. Johnson and T. L. Killeen, pp. 1–21, AGU, Washington D. C., doi:10.1029/GM087p0001.

Roble, R. G., E. C. Ridley, A. D. Richmond, and R. E. Dickinson (1988), A coupled thermosphere/ionosphere general circulation model, *Geophys. Res. Lett.*, *15*, 1325–1328, doi:10.1029/GL015i012p01325.

Solomon, S. C., C. A. Barth, and S. M. Bailey (1999), Auroral production of nitric oxide measured by the SNOE satellite, *Geophys. Res. Lett.*, *26*, 1259–1262, doi:10.1029/1999GL900235.

Solomon, S. C., A. G. Burns, B. A. Emery, M. G. Mlynczak, L. Qian, W. Wang, D. R. Weimer, and M. Wiltberger (2012), Modeling studies of the impact of high-speed streams and co-rotating interaction regions on the thermosphere-ionosphere, *J. Geophys. Res.*, *117*, A00L11, doi:10.1029/2011JA017417.

Sutton, E. K., J. M. Forbes, and R. S. Nerem (2005), Global thermospheric neutral density and wind response to the severe 2003 geomagnetic storms from CHAMP accelerometer data, *J. Geophys. Res.*, *110*, A09S40, doi:10.1029/2004JA010985.

Sutton, E. K., J. M. Forbes, R. S. Nerem, and T. N. Woods (2006), Neutral density response to the solar flares of October and November, 2003, *Geophys. Res. Lett.*, *33*, L22101, doi:10.1029/2006GL027737.

Yonker, J. D. (2013), Contribution of the first electronically excited state of molecular nitrogen to thermospheric nitric oxide, PhD thesis, Virginia Polytech. Inst. and State Univ., Blacksburg, Va.

Yonker, J. D., K. Venkataramani, S. M. Bailey, W. Wang, S. C. Solomon, and C. E. Randall (2014), Updated Chemical, Radiative, and Transport Properties of Thermospheric Odd Nitrogen. Abstracts SA41D-06 presented at 2014 Fall Meeting, AGU, San Francisco, Calif., 15–19 Dec.